

Population III star formation in a Λ WDM universe

Brian W. O'Shea¹ & Michael L. Norman²

ABSTRACT

In this paper we examine aspects of primordial star formation in a gravitino warm dark matter universe with a cosmological constant (Λ WDM). We compare a set of simulations using a single cosmological realization but with a wide range of warm dark matter particle masses which have not yet been conclusively ruled out by observations. The addition of a warm dark matter component to the initial power spectrum results in a delay in the collapse of high density gas at the center of the most massive halo in the simulation and, as a result, an increase in the virial mass of this halo at the onset of baryon collapse. Both of these effects become more pronounced as the warm dark matter particle mass becomes smaller. A cosmology using a gravitino warm dark matter power spectrum assuming a particle mass of $m_{WDM} \simeq 40$ keV is effectively indistinguishable from the cold dark matter case, whereas the $m_{WDM} \simeq 15$ keV case delays star formation in the parent halo by $\simeq 10^8$ years. There is remarkably little scatter between simulations in the final properties of the primordial protostar which forms at the center of the halo, possibly due to the overall low rate of halo mergers which is a result of the WDM power spectrum. The detailed evolution of the collapsing halo core in two representative WDM cosmologies is described. At low densities ($n_b \lesssim 10^5 \text{ cm}^{-3}$), the evolution of the two calculations is qualitatively similar, but occurs on significantly different timescales, with the halo in the lower particle mass calculation taking much longer to evolve over the same density range and reach runaway collapse. Once the gas in the center of the halo reaches relatively high densities ($n_b \gtrsim 10^5 \text{ cm}^{-3}$) the overall evolution is essentially identical in the two calculations.

Subject headings: cosmology: theory — stars: formation — hydrodynamics

¹Theoretical Astrophysics (T-6), Los Alamos National Laboratory, Los Alamos, NM 87545; bwoshea@lanl.gov

²Center for Astrophysics and Space Sciences, University of California at San Diego, La Jolla, CA 92093; mnorman@cosmos.ucsd.edu

1. Introduction

The current canonical view of cosmological structure formation, which assumes that dark matter halos and their contents form in a bottom-up (hierarchical) fashion in a universe with cold dark matter and a cosmological constant (Λ CDM), has been successful in predicting the formation and evolution of large scale structure, as shown in recent years by extensive surveys of the local universe, such as the 2dF and Sloan Digital Sky Survey (Bahcall et al. 1999; Percival et al. 2001; Tegmark et al. 2004). It is acknowledged, however, that there appear to be flaws in the Λ CDM scenario. Observations of the central regions of galaxies show that the central dark matter density of these halos is significantly lower than that predicted by theory (Navarro, Frenk, & White 1997; Navarro et al. 2004; Moore et al. 1999b; Ghigna et al. 2000; Swaters, Madore, & Trewheella 2000; van den Bosch et al. 2000; Dalcanton & Hogan 2001). In addition, the CDM model predicts the formation of a larger number of dwarf galaxies in the local group than is observed (by an order of magnitude), and also suggests that many dwarf galaxies will form in the cosmic voids – a prediction that has not been verified observationally (Moore et al. 1999a; Willman et al. 2004; Klypin et al. 1999; Bode, Ostriker, & Turok 2001; Peebles 2001). In addition there is the “angular momentum” problem of CDM halos, where gas cools at early times into small mass halos, leading to massive, low angular momentum cores in galaxies that are not observed (Sommer-Larsen & Dolgov 2001). The formation of disk-dominated or disk-only galaxies may be impeded by bulge formation in the CDM model due to high merger rates (Governato et al. 2004; Kormendy & Fisher 2005). Finally, there have been observations of significant numbers of dwarf galaxies forming after the larger Lyman break galaxies, which is not what one would expect in a hierarchical clustering scenario (Metcalf et al. 2001). However, at large scales ($\gtrsim 1$ Mpc) the CDM model seems to describe the evolution of the universe and the structure within it quite well.

It is unclear whether the disagreement between the CDM theory of structure formation and current observations is due to an incorrect comparison of simulation and observational data or an absence of essential baryonic processes in the simulations. Kravtsov, Gnedin, & Klypin (2004) suggest that the observed disagreement may be due to incorrectly interpreting dark matter-only simulations, and introduce a model that appears to correctly reproduce the abundance and other properties of observed galactic satellites. Minchin et al. (2005) describe the discovery of an optically dark object in the Virgo cluster found via deep HI survey. This object has a neutral hydrogen gas mass of $\sim 10^8 M_\odot$ and a velocity width of $\Delta V_{20} = 220$ km/s. Measurements of the spatial extent of the object suggest a minimum dynamical mass of $\sim 10^{11} M_\odot$. The Tully-Fisher relation suggests that a galaxy with this velocity width should be 12th magnitude or brighter in optical bands; however, deep imaging has failed to find an optical counterpart down to a surface brightness of 27.5 B mag/arcsec².

The discovery of this object implies the suppression of star formation in galaxy-sized halos, and the authors suggest that a population of these “dark” objects may be found in further deep, high-resolution HI surveys. Finally, Dalal & Kochanek (2002) and Chiba (2002) argue that abundances of inferred dark matter substructure in several galactic lens systems is consistent with predictions in standard CDM models. It is clear that there are aspects of the Λ CDM paradigm that have yet to be fully explored, and disagreements between theory and observation to be reconciled, before cold dark matter can be conclusively ruled out.

If one assumes that there is in fact a flaw with the cold dark matter scenario, the problem is then to devise some physical explanation for the apparent lack of power on small scales while also retaining the desirable qualities of the CDM model on large scales. Many models have been proposed that can provide this suppression. In this paper we discuss the ramifications of a general class of these models, referred to as “warm dark matter,” on the formation of Population III stars. These models predict exponential damping of the linear power spectrum on small length scales (Bardeen et al. 1986; Colombi, Dodelson, & Widrow 1996). The effects of a gravitino warm dark matter cosmology are discussed by Bode et al. (2001), who derive the relevant linear perturbation theory and perform several N-body calculations of warm dark matter cosmologies to understand the general effects of suppression of power on small scales. They find that replacing cold dark matter with warm dark matter results in the smoothing of massive halo cores, which lowers core densities and increases core radii, lowers the characteristic density of low-mass halos, reduces the overall total number of low-mass halos, suppresses the number of low-mass satellite halos in high-mass halos, and results in the formation of low-mass halos almost entirely within caustic sheets or filaments connecting larger halos – voids are almost completely empty, in contrast to CDM. They also find that low-mass halos tend to form at late times, in a top-down process (as opposed to the bottom-up process of halo formation one would expect from a CDM cosmology), and that halo formation is suppressed overall at early times (high redshifts), with an increased evolution of halos at low redshifts relative to the CDM model (this result was later confirmed by Knebe et al. (2003), though see Götz & Sommer-Larsen (2003), who suggest that some of the observed effects are due to inappropriate initial conditions). Furthermore, they argue that constraints based on the observed halo mass function and its evolution suggest that a reasonable minimum warm dark matter particle mass would be 1 keV.

Constraints on the minimum mass of a warm dark matter particle have been placed by various other groups as well. Narayanan et al. (2000) use the clustering properties of Lyman- α forest absorbers to suggest a lower limit of $m_{WDM} = 0.75$ keV. Barkana, Haiman, & Ostriker (2001) use an extended Press-Schechter model to constrain warm dark matter based on observations of cosmological reionization. They calculate that in order for super massive black holes to exist at $z \simeq 6$, and if massive galaxies are responsible for the nearly complete

reionization of the universe by the same redshift, a reasonable minimum mass for a warm dark matter particle is $m_{WDM} \geq 1.2$ keV. Somerville, Bullock, & Livio (2003) observe that the WMAP Year 1 polarization result (Kogut et al. 2003) requires early structure formation and may place a more stringent constraint on m_{WDM} ($\gg 1$ keV). The lowering of the optical depth with the WMAP Year 3 data release (Page et al. 2006) weakens the strength of this argument. Viel et al. (2005) use a combination of WMAP Year 1 and Lyman- α forest power spectrum data to constrain m_{WDM} , finding that $m_{WDM} \gtrsim 550$ eV for early decoupled thermal relics and $m_{WDM} \gtrsim 2$ keV for sterile neutrinos. Finally, Abazajian (2005a) uses a combination of CMB power spectra (from multiple experiments) with 3D galaxy power spectra and 1D Lyman- α forest power spectra from the Sloan Digital Sky Survey to obtain a constraint on the WDM particle mass of $1.7 \text{ keV} < m_s < 8.2 \text{ keV}$, assuming that the warm dark matter particle is a sterile neutrino which suppresses power on small scales in a somewhat different way than the power spectrum described by Bode et al. (2001). The upper limit in this work comes from constraints given by sterile neutrino decay rates (Abazajian, Fuller, & Tucker 2001), and can be disregarded in the gravitino case. The lower limit stated by Abazajian for gravitino dark matter is 0.5 keV (95% CL).

The effects of a warm dark matter particle on the formation of the first generation of stars in the universe may be profound. The WDM particle masses which have not yet been ruled out by observation correspond to mass and spatial scales comparable to those of the halos in which Population III stars form ($M_h \sim 10^6 M_\odot$, $R_h \sim 100$ pc (proper) at $z \sim 20$). WMAP Year 3 observations of CMB polarization implies a significant electron optical depth ($\tau_e = 0.09 \pm 0.03$), which suggests that reionization could have begun at redshifts comparable to the epoch of Pop III star formation in a Λ CDM universe (Page et al. 2006; Abel, Bryan, & Norman 2002; Bromm, Coppi, & Larson 2002). The effect of a warm dark matter particle would generally be to delay the formation of cosmological structure. This has been examined in a statistical way by using techniques such as the extended Press Schechter (EPS) formalism (Somerville et al. 2003), but the details can only be studied accurately with the use of high-resolution numerical simulations.

To this end, Yoshida et al. (2003b) perform N-body+SPH cosmological simulations of structure formation in the early universe of a Λ CDM model and a Λ WDM gravitino model with a warm dark matter particle mass of 10 keV assuming the Bode et al. (2001) transfer function. They find that, as expected, the power spectrum cutoff results in an absence of low-mass halos, which makes the formation of Population III stars very inefficient at redshifts comparable to the epoch of reionization implied by the WMAP Year 1 polarization result. They suggest that, based on this polarization observation, any successful warm dark matter model will have a particle mass greater than 10 keV. Their conclusions, while valid, do not sample the parameter space of allowed warm dark matter particle masses, and the high dark

matter and gas particle masses in their simulations ($m_{DM} \simeq 1000 M_\odot$, $m_b \simeq 160 M_\odot$) do not allow direct examination of the Population III star-forming mass scales. Additionally, the WMAP Year 3 polarization result reduces the strength of their argument concerning limits on the WDM particle mass.

In this paper we address questions raised by Yoshida et al. in a higher level of detail, by both simulating a range of plausible warm dark matter particle masses that have not yet been ruled out by observation and by resolving spatial and mass scales that allow direct examination of the formation of Population III protostellar cloud cores. In Section 2 we discuss Enzo, the adaptive mesh refinement cosmological code used to carry out the simulations (Section 2.1), some general effects of the Bode et al. warm dark matter cosmological model (Section 2.2), and finally the setup of the series of cosmological simulations (Section 2.3). In Section 3 we present our results, first showing some general effects of the variation of the warm dark matter particle mass (Section 3.1), comparing the detailed evolution of the halo cores within two representative warm dark matter models (Section 3.2), and examining the top-down formation of a halo which eventually forms a Population III protostar in a universe with a relatively low WDM particle mass (Section 3.3). Finally, we discuss this work in Section 4 and provide a short summary of results in Section 5.

2. Methodology

2.1. The Enzo code

‘Enzo’¹ is a publicly available, extensively tested adaptive mesh refinement cosmology code developed by Greg Bryan and others (Bryan & Norman 1997a, 1997b; Norman & Bryan 1999; O’Shea et al. 2004, 2005). The specifics of the Enzo code are described in detail in these papers (and references therein), but we present a brief description here for clarity.

The Enzo code couples an N-body particle-mesh (PM) solver (Efstathiou et al. 1985; Hockney & Eastwood 1988) used to follow the evolution of a collisionless dark matter component with an Eulerian AMR method for ideal gas dynamics by Berger & Colella (1989), which allows high dynamic range in gravitational physics and hydrodynamics in an expanding universe. This AMR method (referred to as *structured* AMR) utilizes an adaptive hierarchy of grid patches at varying levels of resolution. Each rectangular grid patch (referred to as a “grid”) covers some region of space in its *parent grid* which requires higher resolution, and can itself become the parent grid to an even more highly resolved *child grid*. Enzo’s im-

¹<http://cosmos.ucsd.edu/enzo/>

plementation of structured AMR places no fundamental restrictions on the number of grids at a given level of refinement, or on the number of levels of refinement. However, owing to limited computational resources it is practical to institute a maximum level of refinement, ℓ_{max} . Additionally, the Enzo AMR implementation allows arbitrary integer ratios of parent and child grid resolution, though in general for cosmological simulations (including the work described in this paper) a refinement ratio of 2 is used.

Since the addition of more highly refined grids is adaptive, the conditions for refinement must be specified. In Enzo, the criteria for refinement can be set by the user to be a combination of any or all of the following: baryon or dark matter overdensity threshold, minimum resolution of the local Jeans length, local density gradients, local pressure gradients, local energy gradients, shocks, and cooling time. A cell reaching any or all of the user-specified criteria will then be flagged for refinement. Once all cells of a given level have been flagged, rectangular solid boundaries are determined which minimally encompass them. A refined grid patch is then introduced within each such bounding volume, and the results are interpolated to a higher level of resolution.

In Enzo, resolution of the equations being solved is adaptive in time as well as in space. The timestep in Enzo is satisfied on a level-by-level basis by finding the largest timestep such that the Courant condition (and an analogous condition for the dark matter particles) is satisfied by every cell on that level. All cells on a given level are advanced using the same timestep. Once a level L has been advanced in time Δt_L , all grids at level $L + 1$ are advanced, using the same criteria for timestep calculations described above, until they reach the same physical time as the grids at level L . At this point grids at level $L + 1$ exchange baryon flux information with their parent grids, providing a more accurate solution on level L . Cells at level $L + 1$ are then examined to see if they should be refined or de-refined, and the entire grid hierarchy is rebuilt at that level (including all more highly refined levels). The timestepping and hierarchy rebuilding process is repeated recursively on every level to the maximum existing grid level in the simulation.

Two different hydrodynamic methods are implemented in Enzo: the piecewise parabolic method (PPM) (Woodward & Colella 1984), which was extended to cosmology by Bryan et al. (1995), and the hydrodynamic method used in the ZEUS magnetohydrodynamics code (Stone & Norman 1992a, 1992b). We direct the interested reader to the papers describing both of these methods for more information, and note that PPM is the preferred choice of hydro method since it is higher-order-accurate and is based on a technique that does not require artificial viscosity, which smoothes shocks and can smear out features in the hydrodynamic flow.

The chemical and cooling properties of primordial (metal-free) gas are followed using

the method of Abel et al. (1997) and Anninos et al. (1997). This method follows the non-equilibrium evolution of a gas of primordial composition with 9 total species: H , H^+ , He , He^+ , He^{++} , H^- , H_2^+ , H_2 , and e^- . The code also calculates radiative heating and cooling following atomic line excitation, recombination, collisional excitation, free-free transitions, molecular line excitations, and Compton scattering of the cosmic microwave background, as well as any of approximately a dozen different models for a metagalactic UV background that heat the gas via photoionization and photodissociation. The multispecies rate equations are solved out of equilibrium to properly model situations where, e.g., the cooling time of the gas is much shorter than the hydrogen recombination time. A total of 9 kinetic equations are solved, including 29 kinetic and radiative processes, for the 9 species mentioned above. The chemical reaction equation network is technically challenging to solve due to the huge range of reaction time scales involved – the characteristic creation and destruction time scales of the various species and reactions can differ by many orders of magnitude. As a result, the set of rate equations is extremely stiff, and an explicit scheme for integration of the rate equations can be costly if small enough timestep are taken to keep the network stable. This makes an implicit scheme preferable for such a set of equations, and Enzo solves the rate equations using a method based on a backwards differencing formula (BDF) in order to provide a stable and accurate solution.

It is important to note the regime in which this chemistry model is valid. According to Abel et al. (1997) and Anninos et al. (1997), the reaction network is valid for temperatures between $10^0 - 10^8$ K. The original model discussed in these two references is only valid up to $n_H \sim 10^4 \text{ cm}^{-3}$. However, addition of the 3-body H_2 formation process allows correct modeling of the gas chemistry up to the point where the optically thin cooling approximation begins to break down, at $\sim 10^{10} - 10^{11} \text{ cm}^{-3}$. Beyond this point, modifications to the cooling function that take into account the non-negligible opacity of the gas to line radiation from molecular hydrogen must be made, as discussed by Ripamonti & Abel (2004). Even with these modifications, a more correct description of the cooling of gas of primordial composition at high densities will require some form of radiation transport, which will greatly increase the cost of the simulations.

2.2. Effects of a gravitino WDM model

As discussed previously, the primary effect of a warm dark matter particle is suppression of the linear power spectrum at small scales. There are currently two favored warm dark matter candidates: gravitinos and sterile neutrinos. We refer readers interested in a discussion of the particle physics motivation for these medium-mass particles, as well as a

discussion of their detailed properties, to work by Bode et al. (2001) and Abazajian (2005b), and references therein. It is useful to note that the power spectrum for these warm dark matter candidates varies (see, e.g. Abazajian (2005b)). The sterile neutrino candidate may have secondary effects which may significantly change the evolution of structure in the early universe (Biermann & Kusenko (2006); see Section 4 for a discussion of this) so for simplicity we choose to use the gravitino warm dark matter of Bode et al. (2001). Due to this, we expect that application of our results to specific warm dark matter particle candidates may require some renormalization of the particle masses, though the results presented in this work should be qualitatively correct for both warm dark matter candidates.

Bode et al. (2001) derive a formula for the power spectrum cutoff due to the existence of a gravitino warm dark matter particle. They provide the following transfer function that models the smoothing of small-scale density perturbations:

$$T_k^X = [1 + (\alpha k)^2]^{-5} \quad (1)$$

Where $\alpha = 0.05(\Omega_{WDM}/0.4)^{0.15}(h/0.65)^{1.3}(keV/m_{WDM})^{1.15}(1.5/g_x)^{0.29}$ and k is in units of $h \text{ Mpc}^{-1}$. In this equation Ω_{WDM} is the contribution of the warm dark matter species to the energy density of the universe, in units of the critical density, m_{WDM} is the gravitino mass in keV, h is the Hubble constant in units of 100 km/s/Mpc, and g_x is a parameter meant to represent the effective number of relativistic species present at decoupling, and is taken to be 1.5. This transfer function is applied on top of the standard CDM transfer function, and imposes a strong rollover in the power spectrum at small scales, corresponding to a spatial smoothing scale of:

$$R_s \simeq 0.31 \left(\frac{\Omega_{WDM}}{0.3} \right)^{0.15} \left(\frac{h}{0.65} \right)^{1.3} \left(\frac{keV}{m_{WDM}} \right)^{1.15} h^{-1} \text{Mpc} \quad (2)$$

This corresponds to the comoving half-wavelength of the mode at which the linear perturbation amplitude is suppressed by a factor of 2. This smoothing results in a characteristic mass scale below which structure forms by the top-down fragmentation of halos, rather than by the bottom-up hierarchical structure formation associated with the cold dark matter paradigm, which can be quantified as:

$$M_s = 10^{10} \left(\frac{\Omega_{WDM}}{0.3} \right)^{1.45} \left(\frac{h}{0.65} \right)^{3.9} \left(\frac{keV}{m_{WDM}} \right)^{3.45} h^{-1} M_\odot \quad (3)$$

Figure 1 contains several panels demonstrating the effects of the warm dark matter cosmology discussed above. Panel (a) shows the cosmological power spectrum $P(k)$ at $z = 0$

for a CDM cosmology as well as for when the WDM transfer function has been applied for several different warm dark matter masses ranging from 0.1 – 100 keV. Panel (b) shows the dimensionless linear power $\Delta^2(k) \sim k^3 P(k)$ with the same particle masses. Panel (c) shows the suppression mass as a function of radius, and panel (d) shows the comoving spatial smoothing scale. In panels (c) and (d), the dashed line indicates the mass and radius corresponding to a halo of mass $4 \times 10^5 M_\odot$, which is roughly the mean halo mass for a suite of simulations of Population III star formation in a Λ CDM universe (O’Shea & Norman 2006, in preparation). Note that this mass scale, which corresponds to a gravitino mass of $\simeq 15$ keV, is consistent with previous estimates, given some ambiguity in the definition of the halo mass and collapse epoch and details of the initial simulation setup in different studies (Tegmark et al. 1997; Machacek, Bryan, & Abel 2001; Bromm et al. 2002; Yoshida et al. 2003a).

2.3. Simulation setup

The simulations discussed in this paper are set up as follows. A dark matter-only calculation with 128^3 particles in a three-dimensional simulation volume which is $0.3 h^{-1}$ Mpc (comoving) on a side is set up at $z = 99$ assuming a “concordance” cosmological model with no baryons: $\Omega_m = \Omega_{DM} = 0.3$, $\Omega_b = 0.0$, $\Omega_\Lambda = 0.7$, $h = 0.7$ (in units of 100 km/s/Mpc), $\sigma_8 = 0.9$, and using an Eisenstein & Hu power spectrum (Eisenstein & Hu 1999) with a spectral index of $n = 1$. The cold dark matter cosmological model is assumed. This calculation is then evolved to $z = 15$ using a maximum of four levels of adaptive mesh refinement, refining on a dark matter overdensity of 8.0. At $z = 15$, the Hop halo finding algorithm (Eisenstein & Hut 1998) is used to find the most massive halo in the simulation.

At this point, we generate several sets of initial conditions with the same large-scale structure by smoothing the CDM initial conditions described above with the warm dark matter transfer function described by Equation 1, assuming $\Omega_b = 0.04$, $\Omega_{WDM} = \Omega_{DM} = 0.26$, $g_x = 1.5$, and warm dark matter particle masses of $m_{WDM} = 10, 12.5, 15, 17.5, 20, 25, 30, 35$, and 40 keV. All other cosmological parameters are identical. An additional calculation is performed with identical parameters but assuming the CDM model ($m_{WDM} = \infty$). The initial conditions are generated with both dark matter and baryons such that the Lagrangian volume in which the halo in the CDM case formed is resolved at high spatial and mass resolution using a series of static nested grids, with a 128^3 root grid and three static nested grids, for an overall effective root grid size of 1024^3 cells. The highest resolution grid is 256^3 grid cells, and corresponds to a volume $75 h^{-1}$ comoving kpc on a side. The dark matter particles in the highest resolution grid are $1.81 h^{-1} M_\odot$ and the spatial resolution

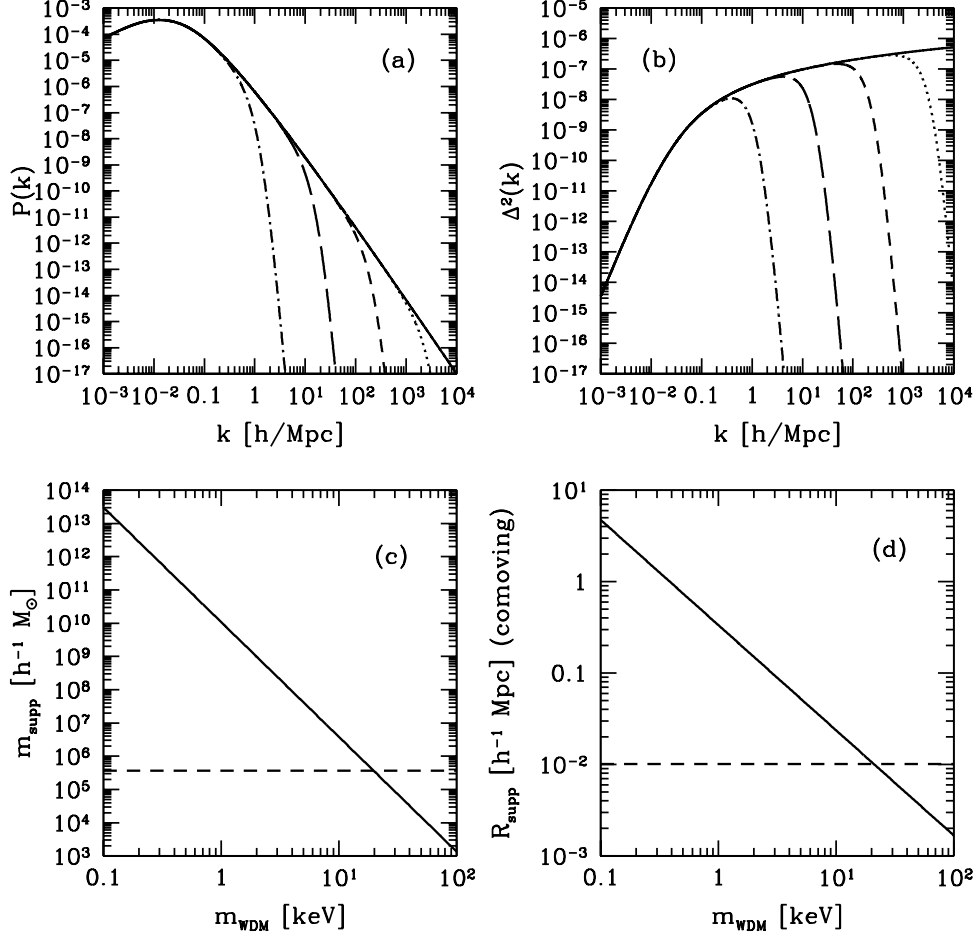


Fig. 1.— Plots showing various effects of a gravitino warm dark matter particle. Panel (a): The $z = 0$ dark matter power spectrum $P(k)$ as a function of wavenumber $k \equiv 2\pi/\lambda$ for a CDM cosmology and a range of warm dark matter masses. Panel (b): The $z = 0$ dimensionless power, $\Delta^2(k) \sim k^3 P(k)$, versus k . Panel (c): The “suppression mass” as a function of WDM particle mass. Panel (d): The spatial “smoothing scale” as a function of WDM particle mass. In plots (a) and (b) the solid line corresponds to a CDM universe and the dotted, short dashed, long dashed and dot-short dashed lines correspond to cosmologies with gravitino masses of $m_{\text{WDM}} = 100, 10, 1$ and 0.1 keV, respectively. In plots (c) and (d) the horizontal dashed line indicates the mass and radius corresponding to a halo of mass $4 \times 10^5 M_{\odot}$, which is approximately the mean halo mass from a set of adaptive mesh refinement calculations of Population III star formation in a Λ CDM universe (O’Shea & Norman 2006, in preparation).

of the highest resolution grid is 293 h^{-1} parsecs (comoving). Previous work shows that this particle mass resolution is more than adequate to fully resolve the collapse of the halo (Abel, Bryan & Norman, 2002; O’Shea & Norman 2006, in preparation).

All simulations are performed using the adaptive mesh cosmology code Enzo, which is described in Section 2.1. The simulations are started at $z = 99$ and allowed to evolve until the collapse of the gas within the center of the most massive halo. The equations of hydrodynamics are solved using the PPM method with a dual energy formulation which is required to adequately resolve the thermal properties of gas in high-Mach flows. The nonequilibrium chemical evolution and optically thin radiative cooling of the primordial gas is modeled as described in Section 2.1, following 9 separate species including molecular hydrogen (but excluding deuterium), with an initial electron fraction of 1.2×10^{-5} (which is roughly consistent with Peebles (1968)). Note that the initial electron fraction in the calculation is relatively unimportant to the molecular hydrogen formation rates in halo cores, as the electron fraction at the center of a given halo is controlled primarily by mergers and the shock formed by accretion of gas onto the halo.

Adaptive mesh refinement is used such that cells are refined by factors of two along each axis, with a maximum of 22 total levels of refinement. This corresponds to a maximum spatial resolution of 115 h^{-1} astronomical units (comoving) at the finest level of resolution, with an overall spatial dynamical range of 5.37×10^8 . To avoid effects due to the finite size of the dark matter particles, the dark matter density is smoothed on a comoving scale of $\sim 0.5 \text{ pc}$ (which corresponds to $\simeq 0.03$ proper pc at $z \simeq 18$). This is reasonable because at that radius in all of our calculations the gravitational potential is completely dominated by the baryons.

Grid cells are adaptively refined based upon several criteria: baryon and dark matter overdensities in cells of 4.0 and 8.0, respectively, as well as criteria to ensure that the pressure jump and/or energy ratios between adjoining cells never exceeds 5.0, that the cooling time in a given cell is always longer than the sound crossing time of that cell, and that the Jeans length is always resolved by at least 16 cells. This last criterion guarantees that the Truelove criterion (Truelove et al. 1997) is always resolved by a factor of four more cells in each dimension than is strictly necessary, ensuring that no artificial fragmentation will take place.

3. Results

3.1. General results

In this section we present the results of a comparison of all of the warm dark matter simulations, along with the cold dark matter “control” simulation. Figure 2 shows bulk properties of the halo in which the Population III protostar forms as a function of the warm dark matter particle mass. The top left and right panels plot the WDM particle mass versus the redshift (left) and time after the Big Bang (right) at which the halo core collapses (where “collapse” in this paper is defined as when the central baryon density of the halo reaches $\sim 10^{10} \text{ cm}^{-3}$). The CDM result is shown in both panels by a vertical dashed line. Clearly, decreasing the warm dark matter particle mass delays the formation of the protostar. The 40 keV calculation forms at essentially the same time as the CDM simulation, while collapse of the halo core in the calculation assuming a 12.5 keV WDM particle mass is delayed by approximately 130 million years compared to the CDM result. The simulation with a 10 keV particle mass does not collapse by $z = 10$ (the end of the simulation) and is not shown here. The delay of the halo collapse appears to be generally smoothly varying as a function of WDM particle mass.

The bottom left panel of Figure 2 shows the virial mass of the halo (at the redshift of collapse) as a function of WDM particle mass. A reduction in the WDM particle mass leads to an increase in the halo virial mass, which is related to the delay in collapse of the halo core – by the time the halo core collapses in the lower particle mass simulations, the halo has had time to accrete more mass. The bottom right panel of Figure 2 shows the dark matter spin parameter of each halo (at the time of core collapse) as a function of the gravitino particle mass. It is clear that there is a relationship between halo mass and spin parameter, but the overall cause and implications are unclear. The gas spin parameter (not shown) displays similar behavior.

Figures 3 and 4 show several spherically-averaged, mass-weighted radial profiles of baryon quantities as a function of radius or enclosed baryon mass of the simulations. All profiles are taken at a constant point in the evolution of the protostellar cloud (when the proper central baryon number density is $n \sim 10^{10} \text{ cm}^{-3}$) rather than at a constant point in time, since the halos collapse over a wide range of redshifts. Figure 3 shows the proper baryon number density as a function of enclosed baryon mass (Panel (a)), baryon temperature as a function of enclosed baryon mass (Panel (b)), molecular hydrogen fraction as a function of enclosed baryon mass (Panel (c)), and enclosed baryon mass as a function of radius (Panel (d)). As expected, the number density profiles of all of the simulations are very similar over the entire range of WDM (and CDM) particle masses. This is a result

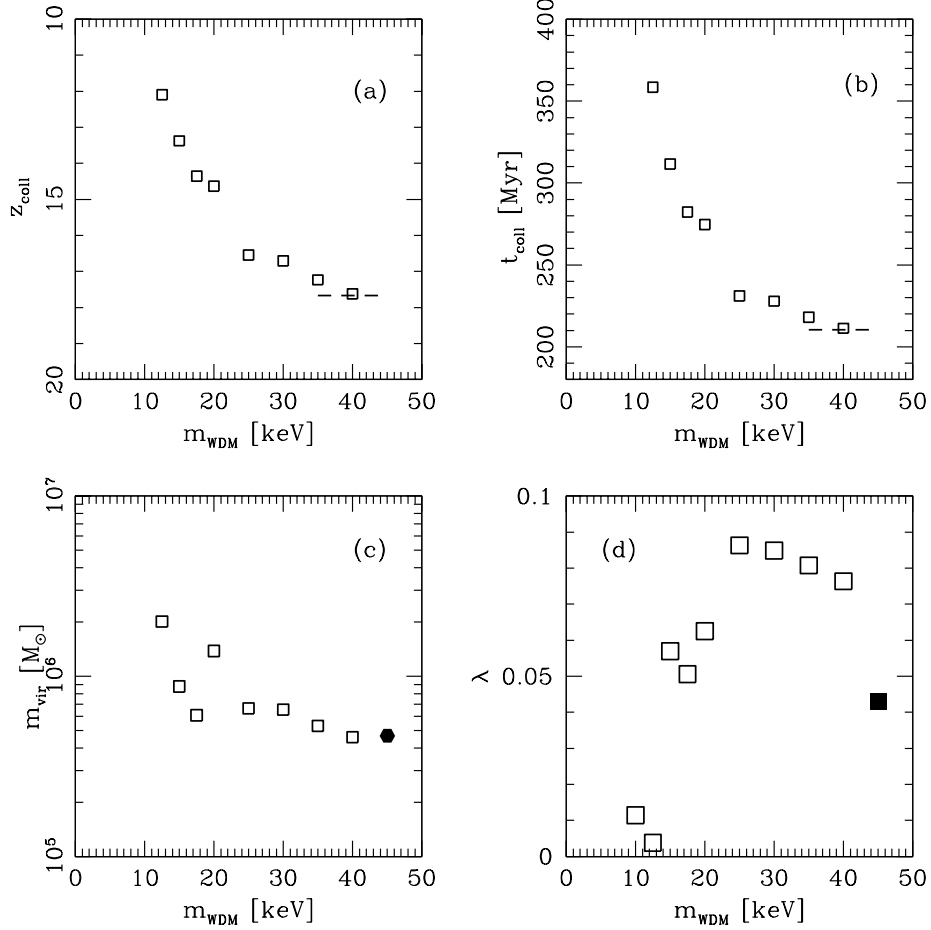


Fig. 2.— Dark matter halo properties as a function of WDM particle mass for several simulations with the same cosmological realization but different warm dark matter particle masses. Panel (a): WDM particle mass vs. collapse redshift of halo core. Panel (b): WDM particle mass vs. collapse time of halo core (measured in millions of years after the Big Bang). Panel (c): halo virial mass at collapse vs. WDM particle mass. Panel (d): halo dark matter spin parameter at collapse vs. WDM particle mass. In panels (a) and (b) the collapse redshift/time of the cold dark matter (CDM) simulation is shown by a horizontal dashed line. In panel (c) the virial mass of the halo in the CDM simulation is shown by a solid circle, while the WDM simulations are represented by open squares. In panel (d) the spin parameter of the halo in the CDM simulation is shown by a solid square, while the WDM simulations are represented by open squares.

of the cooling properties of the gas. In the absence of any other sources of energy (such as magnetic fields or cosmic rays), self-gravitating gas in pressure equilibrium tends toward an isothermal (r^{-2}) density profile, which is seen here. The simulation assuming a WDM particle mass of 10 keV does not collapse by the time the simulation is stopped at $z = 10$, and the density profile at the last output time is shown. The plot of enclosed mass as a function of radius shows a strong similarity between the different calculations as well, which is to be expected as it is essentially another way of viewing the number density plot. The plots of temperature and molecular hydrogen fraction vs. enclosed mass show a significant amount of scatter. Ignoring the 10 keV case, the overall spread in temperature in the core of the halo is a factor of ~ 3 and the spread in molecular hydrogen fraction is roughly 1.5 orders of magnitude. It is interesting to note that the CDM “control” simulation has one of the higher core temperatures and a median H_2 fraction. There is no apparent relationship between the warm dark matter particle mass and final baryon quantities.

Figure 4 shows the specific angular momentum as a function of enclosed baryon mass (Panel (a)), circular velocity as a function of radius (Panel (b)), radial velocity as a function of enclosed baryon mass (Panel (c)), and accretion time as a function of enclosed baryon mass (Panel (d)). The angular momentum distributions are somewhat similar for all of the calculations (disregarding the 10 keV case since it does not collapse), though there is a great deal of scatter at large radii, which is also shown in the scatter in spin parameter in Figure 2 (d). The circular velocities are similar as well, though also with a noticeable scatter. The Keplerian orbital velocity for the CDM (least massive) halo is plotted in this panel (upper thin black line), and all of the simulations display circular velocities that are significantly below this velocity. The plot of radial velocity as a function of enclosed baryon mass shows that the CDM simulation has the greatest infall velocity at the output time in question, which corresponds to the largest accretion rate overall (as shown in the plot of accretion time vs. enclosed baryon mass). The rest of the calculations have similar infall velocities and accretion rates, except for the 15 keV model, which has a much lower overall infall velocity and accretion rate. The reason for this is unclear. The overall accretion rates for the WDM calculations are slightly less than that of the CDM calculation, suggesting that the final stellar masses may be slightly lower, if one applies the same techniques for estimating the stellar mass as used by Abel et al. (2002). However, it has been argued that the magnitude of the accretion rate onto a primordial protostar at the time of core collapse may not be directly related to the final mass (Omukai & Palla 2003), so the effect of the change of accretion rates is unclear.

Figure 5 shows the evolution of clumping factor as a function of redshift for the CDM case (solid black line) and four representative gravitino particle masses: 12.5, 20, 30 and 40 keV. In the other quantities, the 40 keV run is almost indistinguishable from CDM, while

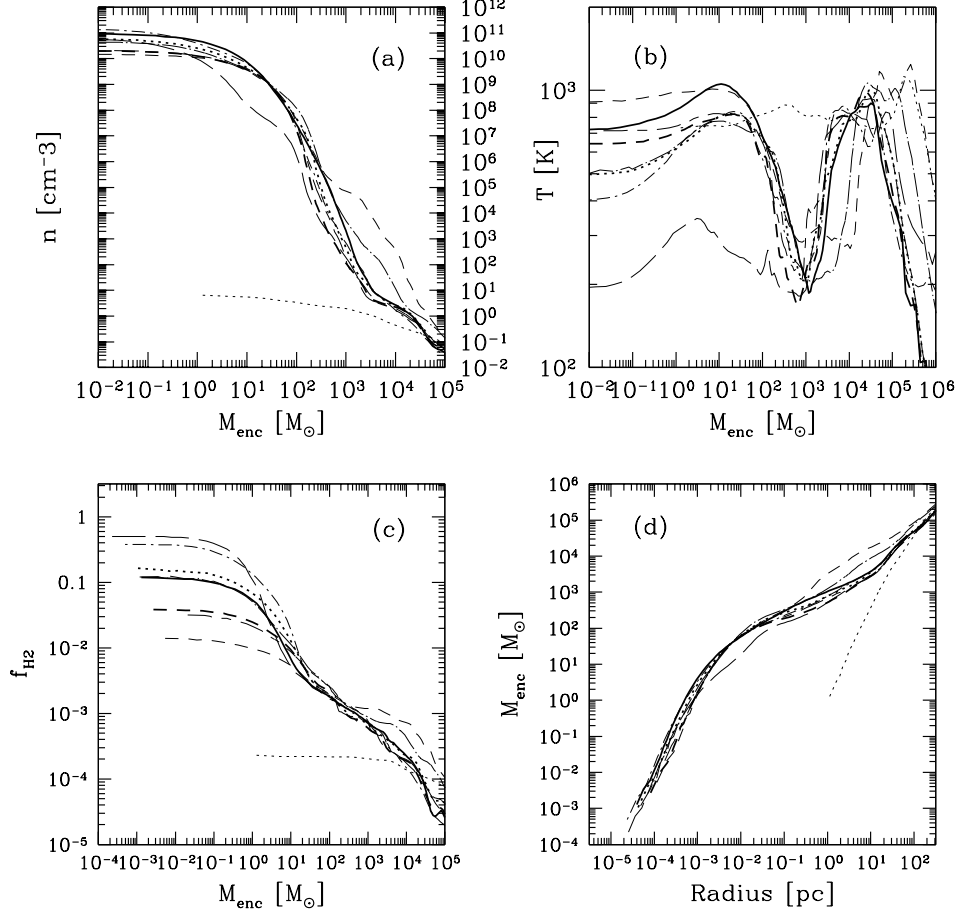


Fig. 3.— Mass-weighted, spherically-averaged baryon quantities for several simulations with the same cosmological realization but different warm dark matter particle masses. Panel (a): baryon number density as a function of enclosed baryon mass. Panel (b): baryon temperature as a function of enclosed baryon mass. Panel (c): molecular hydrogen fraction as a function of enclosed baryon mass. Panel (d): enclosed baryon mass as a function of radius. Output times are chosen such that the peak baryon density in each simulation is approximately the same. In each panel, the CDM simulation is represented by a thick solid line. The 10, 12.5, 15, 17.5, 20, and 25 keV simulations are represented by thin dotted, short-dashed, long-dashed, dot short-dashed, dot long-dashed, and short dash-long dashed lines, respectively. The 30 and 35 keV calculations are represented by thick dotted and short-dashed lines, respectively.

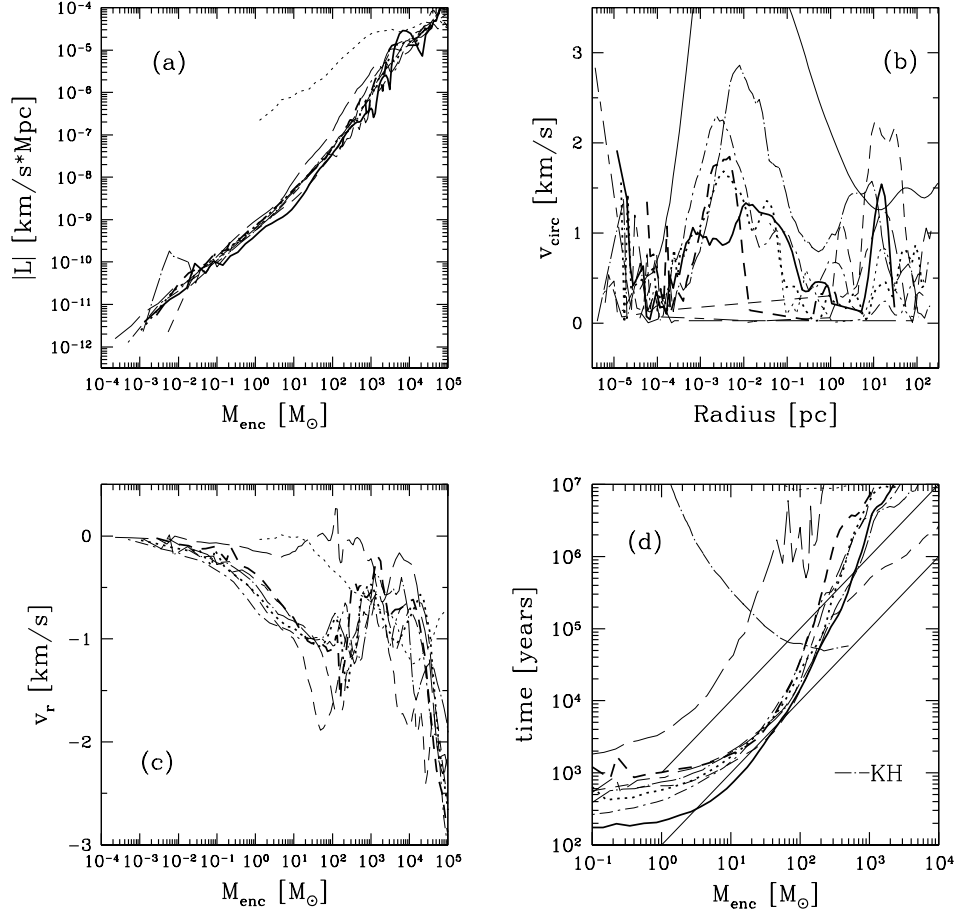


Fig. 4.— Mass-weighted baryon quantities for several simulations with the same cosmological realization but different warm dark matter particle masses. Panel (a): spherically-averaged baryon angular momentum as a function of enclosed baryon mass. Panel (b): cylindrically-averaged circular velocity a function of radius. Panel (c): spherically-averaged radial velocity as a function of enclosed baryon mass. Panel (d): spherically-averaged accretion rate as a function of enclosed baryon mass. Output times are chosen such that the peak baryon density in each simulation is approximately the same. Line types are the same as in Figure 3. The $m_{\text{WDM}} = 10$ keV case does not collapse by the end of the simulation and is shown at the last available output time in panels (a)-(c), and not shown in panel (d). In Panel (d) the dot-long dashed line which is roughly perpendicular to the others is the Kelvin-Helmholtz time calculated from Population III stellar properties from Schaerer (2002) and the upper and lower diagonal thin solid lines correspond to constant accretion rates of 10^{-3} and $10^{-2} M_{\odot}/\text{yr}$, respectively.

lowering the gravitino particle mass decreases the clumping factor for a given redshift. This may have implications for reionization, though the simulation volume is too small to draw meaningful statistical conclusions (as discussed in Section 4).

3.2. Comparison of two representative models

In this section we compare the evolution of two representative warm dark matter simulations. We choose the calculations with WDM particle masses of 12.5 and 25 keV, as these are examples of simulations where the warm dark matter “suppression mass” is somewhat above (12.5 keV) or below (25 keV) the mean CDM Population III halo mass of $\simeq 4 \times 10^5 M_\odot$, suggesting that these halos will form via top-down fragmentation or hierarchical mergers, respectively, and a comparison of the primordial protostellar core’s properties in each case will be illuminating. Figure 6 shows mass-weighted projections of dark matter density, baryon density, and baryon temperature at $z = 20.38$ for the two representative WDM calculations and a CDM calculation of the same cosmological realization. All panels show a volume that is ~ 300 pc (proper) across and are centered on the point in space where the first Population III protostar will form. There is a significant difference between the calculations at a fixed point in time – the cold dark matter calculation (right column) shows a great deal of clumpy dark matter structure, including knots along the cosmological filaments and even dark matter halos in void regions, with corresponding variety in the baryon density and temperature plots. The 25 keV calculation shows the effects of smoothing – two halos are forming, but there are no halos in the voids, and no substructure around the halos that form. This is reflected in the baryon temperature and density plots, where the accretion shocks onto the filaments show little small-scale structure and the gas is quite smooth. The 12.5 keV calculation is an even more striking example of the effects of suppressing the power spectrum at small scales – though an overdensity in the dark matter is apparent, no halos are visible at this redshift and there is no smaller scale structure whatsoever. This warm dark matter particle mass corresponds to a smoothing scale of a few times $10^6 M_\odot$, below which it has been speculated that top-down fragmentation takes place (as observed by Knebe et al. (2003), though this has been contested by Götz & Sommer-Larsen (2003)), and is roughly equivalent to the mass of the coalescing halo shown in this image.

Figure 7 shows the same quantities and spatial volume as Figure 6, though instead of the outputs all being at the same point in time, they are at the time when the halo core collapses in each simulation. This corresponds to $z = 18.001$ for the CDM calculation, $z = 16.54$ for the WDM calculation with $m_{WDM} = 25$ keV, and $z = 12.09$ for the WDM calculation with $m_{WDM} = 12.5$ keV. At the time of collapse the 12.5 keV calculation has formed a halo

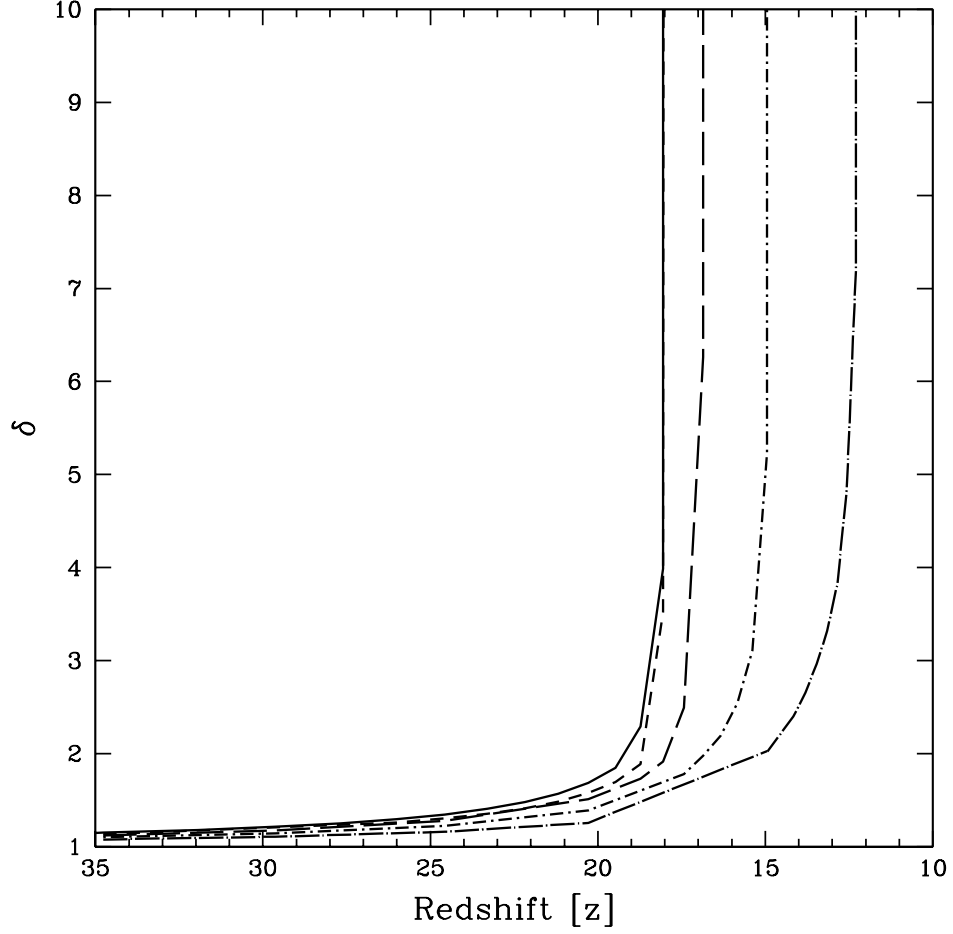


Fig. 5.— Clumping factor as a function of redshift for representative warm dark matter models. The CDM calculation is represented by a black solid line. The $m_{WDM} = 12.5, 20, 30$ and 40 keV models are represented by dot-long-dashed, dot-short-dashed, long-dashed, and short-dashed lines, respectively.

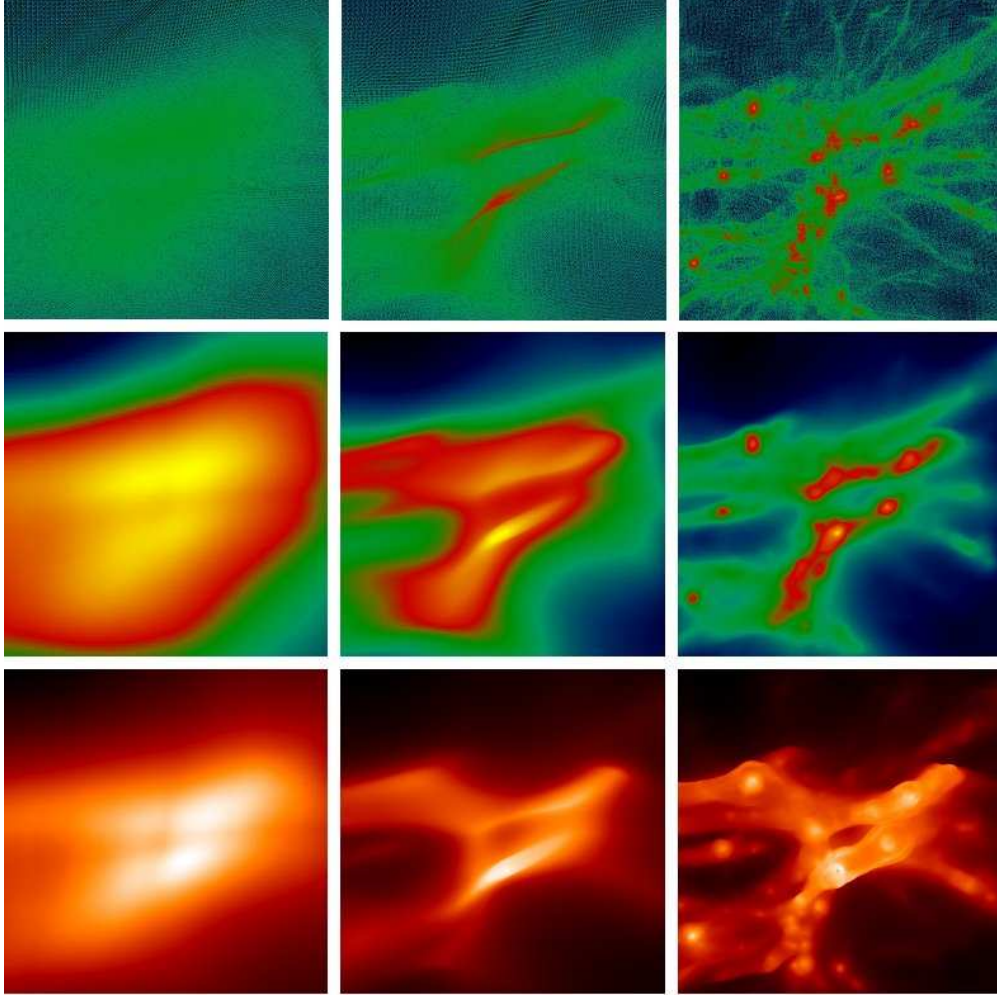


Fig. 6.— Mass-weighted projections of dark matter density, baryon density and baryon temperature for 3 simulations with the same cosmological realization and a range of warm dark matter (WDM) particle masses at $z = 20.38$. The field in each calculation is the same, though the color tables are relative for each panel in order to highlight density differences. Left column: $m_{WDM} = 12.5$ keV. Center column: $m_{WDM} = 25$ keV. Right column: Cold dark matter realization (corresponds to $m_{WDM} \rightarrow \infty$). Top row: projected dark matter density. Middle row: projected baryon density. Bottom row: projected, mass-weighted baryon temperature. The spatial scale is ~ 1.3 kpc (proper) in each volume.

which is more massive than the CDM halo by a factor of ~ 5 (and collapses approximately 130 million years later). Very little substructure is evident in the projected dark matter distribution of the 12.5 keV calculation. Some is apparent in the 25 keV run, but not nearly as much as in the CDM calculation. As predicted by Bode et al. (2001), the warm dark matter calculations have suppressed substructure and satellite halos, and it is apparent that the halo in the 12.5 keV calculation forms by top-down fragmentation of a filament rather than hierarchical merging of smaller halos. This top-down fragmentation results in a great deal of turbulent gas motion – the results of this can be seen in the projected baryon density and temperature plots in the left column of Figure 7, and are discussed in more detail in Section 3.3.

Figures 8 through 10 show the time evolution of several spherically averaged, mass-weighted radial quantities for the two representative warm dark matter calculations. The plots are chosen such that the central densities of the collapsing halo core are matched between the two calculations.

Figure 8 shows the evolution of number density as a function of enclosed mass for the 12.5 keV and 25 keV WDM calculations. The lowest-density line corresponds to $z = 13.16$ for the 12.5 keV run and $z = 18.05$ for the 25 keV calculation. Intriguingly, it takes the 12.5 keV calculation roughly 4×10^7 years to advance from a core number density of $n \sim 10 \text{ cm}^{-3}$ (proper) to a core baryon number density of $n \sim 10^5 \text{ cm}^{-3}$, while the 25 keV calculation only requires $\sim 2 \times 10^7$ years to evolve over the same range. However, once the calculations reach $\simeq 10^5 \text{ cm}^{-3}$ they take similar amounts of time to evolve to the highest number density shown. As discussed in previous sections, this reflects the fact that the halo evolution on small scales is controlled by the chemistry and cooling properties of the primordial gas, which is unaffected by the dark matter properties. The slower evolution of the gas in the $m_{WDM} = 12.5 \text{ keV}$ simulation at low densities can be attributed to the top-down formation of the halo – the halo’s potential well is shallower overall (due to its more extended dark matter profile), leading to a shallower baryon density profile at the halo core and thus longer chemical reaction times and slower core evolution.

Figure 9 shows the evolution of baryon temperature and molecular hydrogen fraction as a function of enclosed mass for the two warm dark matter simulations. The overall temperature evolution is very similar between the two calculations, though the calculation with $m_{WDM} = 12.5 \text{ keV}$ ends up with a slightly lower molecular hydrogen fraction and slightly higher central temperature. The evolution of radial infall velocity and angular momentum as a function of enclosed mass (shown in Figure 10) is also quite similar between the two calculations. As shown in Figure 4, the final accretion rates are also essentially the same.

The purpose of this section was to demonstrate that the evolution of the halo collapse,

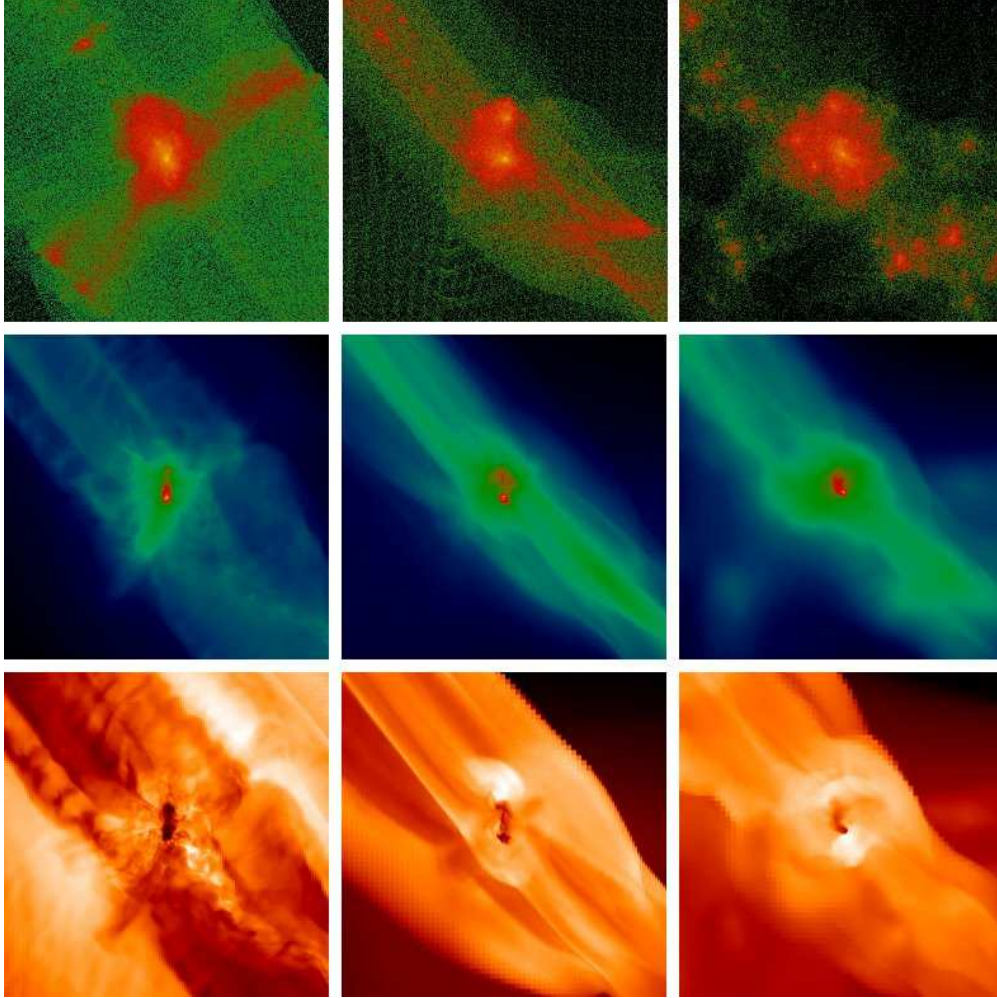


Fig. 7.— Mass-weighted projections of dark matter density, baryon density and baryon temperature for 3 simulations with the same cosmological realization and a range of warm dark matter (WDM) particle masses at the redshift at which the Population III protostar collapses in each simulation. The comoving size of the projected volume in each calculation is the same, though the color tables are relative for each panel in order to highlight density differences. Left column: $m_{WDM} = 12.5$ keV, $z_{coll} = 12.09$. Center column: $m_{WDM} = 25$ keV, $z_{coll} = 16.54$. Right column: Cold dark matter realization (corresponds to $m_{WDM} \rightarrow \infty$), $z_{coll} = 18.001$. Top row: projected dark matter density. Middle row: projected baryon density. Bottom row: projected baryon temperature. The spatial scale is ~ 300 pc (proper) for the CDM and $m_{WDM} = 25$ keV WDM simulations and ~ 450 pc (proper) for the $m_{WDM} = 12.5$ keV WDM simulation; the comoving scales are the same in each panel.

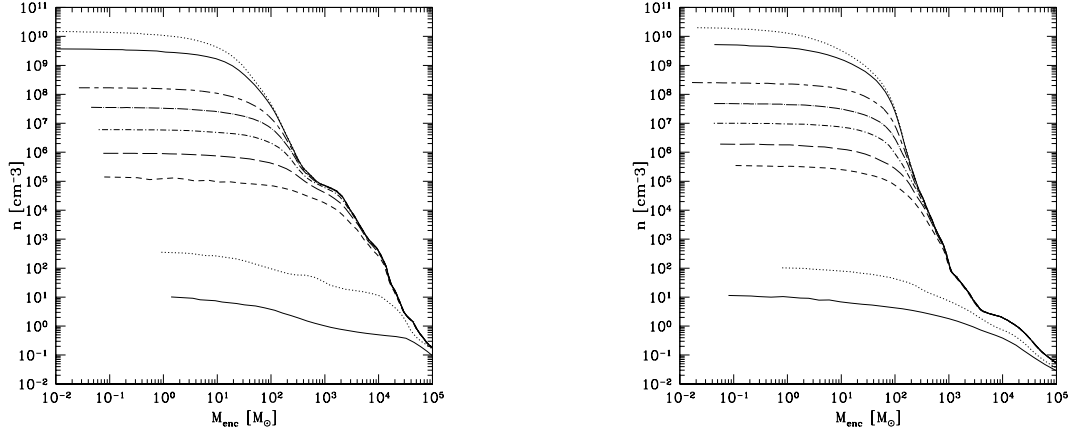


Fig. 8.— Evolution of spherically-averaged, mass-weighted baryon number density as a function of enclosed mass in halos with two representative warm dark matter simulations. The cosmological realization is the same for each calculation, and output times are chosen such that the baryon densities are approximately the same. Left column: simulation with $m_{WDM} = 12.5$ keV. Right column: simulation with $m_{WDM} = 25$ keV. Lines for the $m_{WDM} = 12.5$ keV (25 keV) simulations as follows. Thin solid line: $t = 319$ Myr/ $z = 13.163$ ($t = 204$ Myr/ $z = 18.05$). Thin dotted line: 3.12×10^7 years later (1.04×10^7 years later). Thick short-dashed line: 8.15×10^6 years later (1.04×10^6 years later). Thick long-dashed line: 98,345 years later (5.73×10^6 years later). Thick dot-short-dashed line: 2.86×10^5 years later (2.63×10^5 years later). Thick dot-long-dashed line: 1.25×10^5 years later (82,433 years later). Thick short dashed-long dashed line: 45,152 years later (38,738 years later). Thick solid line: 22,697 years later (24,865 years later). Thick dotted line: 2691 years later (3332 years later).

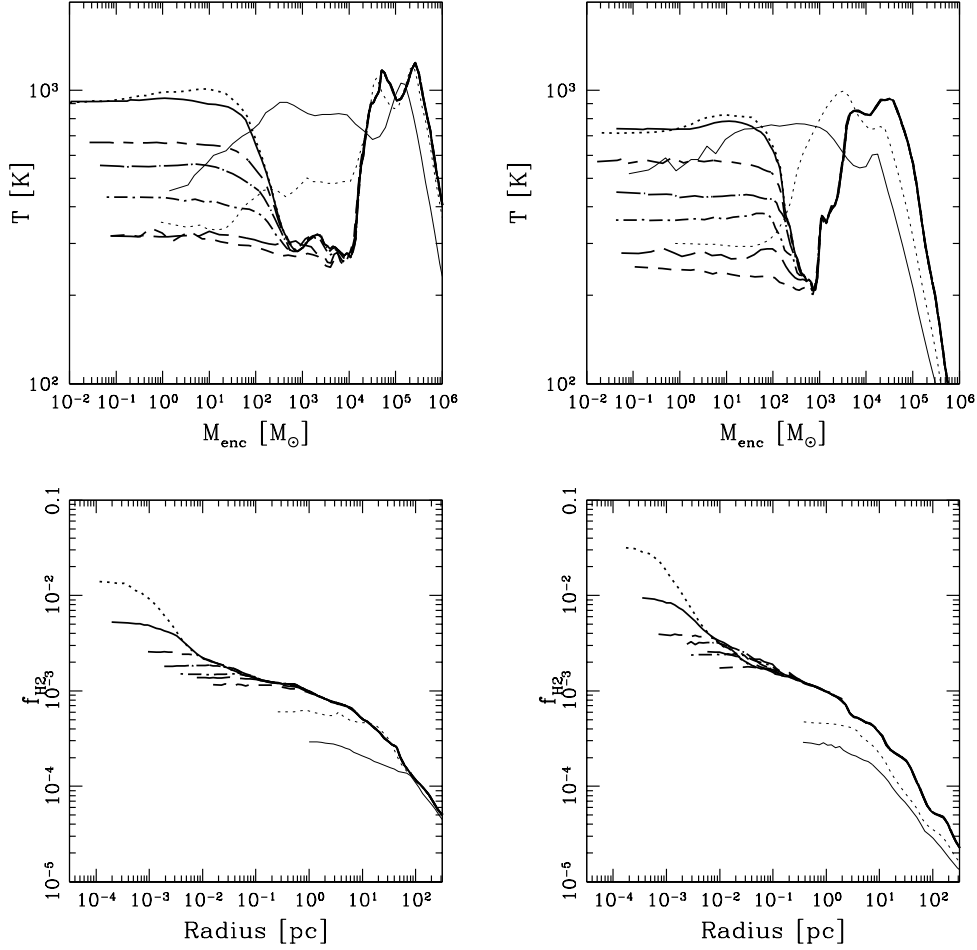


Fig. 9.— Evolution of spherically-averaged, mass-weighted baryon temperature (top row) and molecular hydrogen fraction (bottom row) as a function of enclosed mass in halos with two representative warm dark matter simulations. The cosmological realization is the same for each calculation, and output times are chosen such that the baryon densities are approximately the same. Left column: simulation with $m_{\text{WDM}} = 12.5$ keV. Right column: simulation with $m_{\text{WDM}} = 25$ keV. The lines are at the same times as in Figure 8.

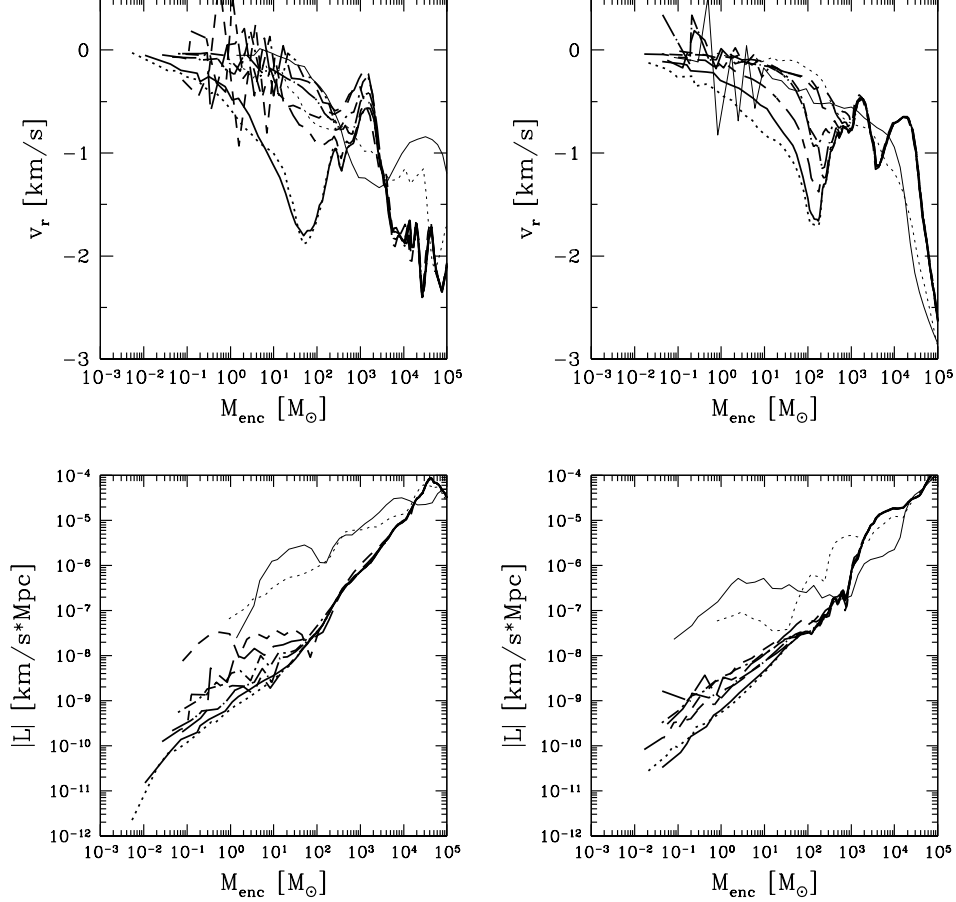


Fig. 10.— Evolution of spherically-averaged, mass-weighted baryon properties in halos with two representative warm dark matter simulations. The cosmological realization is the same for each calculation, and output times are chosen such that the baryon densities are approximately the same. Left column: simulation with $m_{\text{WDM}} = 12.5$ keV. Right column: simulation with $m_{\text{WDM}} = 25$ keV. Top row: baryon radial velocity as a function of enclosed baryon mass (velocity is positive away from the center of the halo). Bottom row: baryon angular momentum as a function of enclosed mass. The lines are at the same times as in Figure 8.

and the resulting protostar, is quite similar for two simulations with significantly different warm dark matter particle masses. The large-scale structure evolves somewhat differently in these two cases – the halo that forms in the 12.5 keV calculation is approximately the same mass scale as the suppression mass, meaning that this dark matter halo is roughly the smallest object that can directly form at that mass scale. The halo that forms in the 25 keV WDM model is significantly larger than the suppression mass, implying that it formed out of the merging of smaller objects. Despite this, the final protostellar properties are similar, which is due to the collapse dynamics being controlled at small scales primarily by the cooling properties of the primordial gas rather than by the dynamics of the large scale cosmological structure.

3.3. Top-down formation of a Population III star-forming halo

Figure 6 (discussed in Section 3.2) shows evidence for significant turbulent gas motion in the halo which forms a Population III star in a $m_{wdm} = 12.5$ keV universe. The gas which appears to be experiencing this turbulent motion is aligned with the filament out of which the cosmological minihalo coalesced, suggesting some sort of large-scale motion is the cause of the turbulence. This sort of structure is not seen in our standard CDM calculation, nor in the $m_{wdm} = 25$ keV run. The “smoothing mass” (the mass corresponding to the spatial scale at which the power spectrum is suppressed by a factor of two compared to CDM) of the 12.5 keV calculation is a few times $10^6 M_\odot$, which is approximately the virial mass of the halo that eventually forms, whereas the same mass scale for the 25 keV calculation is $\simeq 10^5 M_\odot$, and is zero for CDM (by definition). This suggests that the halo in which the Population III star forms in the $m_{WDM} = 12.5$ keV calculation is the smallest object which can form, and should collapse as a single entity rather than being built up through hierarchical merging. How does this affect the properties of the baryons within the halo?

Figure 11 shows images of projected baryon density and temperature taken at three different times during the collapse of this halo. The top row shows the halo at a point in time shortly after it has become a distinct object. In contrast to a CDM Population III minihalo, the halo structure is greatly elongated and it appears that a caustic of some sort is beginning to form. Examination of the baryon temperatures show that gas has not yet been shocked to high values. The center row shows the halo at a later time ($\sim 6 \times 10^7$ years later), when the baryons have collapsed further. The collapse occurs along the minor axis of the halo, and has heated the gas to relatively high temperatures. A cylindrical shock structure can be clearly seen at both large and small scales (center and right columns), and turbulent structures can be seen in regions of high baryon density. Due to the cylindrical collapse of

the halo, these structures are generally aligned with the filament. The bottom row shows the halo at the time when the Population III protostellar core reaches central baryon densities of $\sim 10^{10} \text{ cm}^{-3}$, approximately 5×10^7 years after the previous row of images. Turbulent structures aligned with the filament are clearly visible, as is the shocked gas in the halo.

Figure 12 shows the evolution of the turbulent structures in a more quantitative fashion. This figure shows the time evolution of the cylindrically-averaged baryon number density, temperature, radial velocity, and 3D RMS velocity over the range of times shown in Figure 11. The cylindrical average is calculated with respect to the center of the cosmological filament at each timestep shown, with the cylinder aligned with the filament, and examining all gas with a proper density $\gtrsim 10^{-2} \text{ cm}^{-3}$. The halo is initially collapsing with a strong radial velocity and some non-radial motion (as can be seen by the 3D RMS velocity). Over time, as the halo collapses and gas shocks, the disordered (i.e. turbulent) motion of the gas increases, as can be seen by the large increase of gas RMS velocity with respect to the radial velocity. Examination of the temperature evolution of the gas shows an object which was initially generally quite cool, but was heated at large radii and late times by the same large-scale shocks that created the turbulent gas motions.

4. Discussion

There are several effects which we have neglected in these calculations which may affect our results. The box size of the calculations presented in this paper is relatively small (300 kpc/h comoving). Barkana & Loeb (2004) show that finite box sizes can have significant effects on statistical properties of halo formation, resulting in an overall bias towards undersampling of the mass function and late halo formation times. Though their results were explicitly for a CDM cosmology, they are also relevant for warm dark matter cosmologies. However, our calculations are not intended to provide a statistically accurate sampling of the mass function of dark matter halos. Rather, the intent is to gain a qualitative feel for the effects of a warm dark matter power spectrum on a single halo. An obvious extension of this work would be to simulate a much larger box size so that cosmic variance and possible halo environmental effects are considered (as discussed in Barkana & Loeb (2004)), and then simulate multiple halos within these boxes for a range of Λ WDM models, all compared to a Λ CDM “control” calculation. A suite of simulations such as these is computationally costly, but not completely infeasible, and would lend statistical weight to the qualitative results presented in this work.

Another important consideration is the generalization of cosmological initial conditions. Götz & Sommer-Larsen (2003) show that grid-based warm dark matter initial conditions

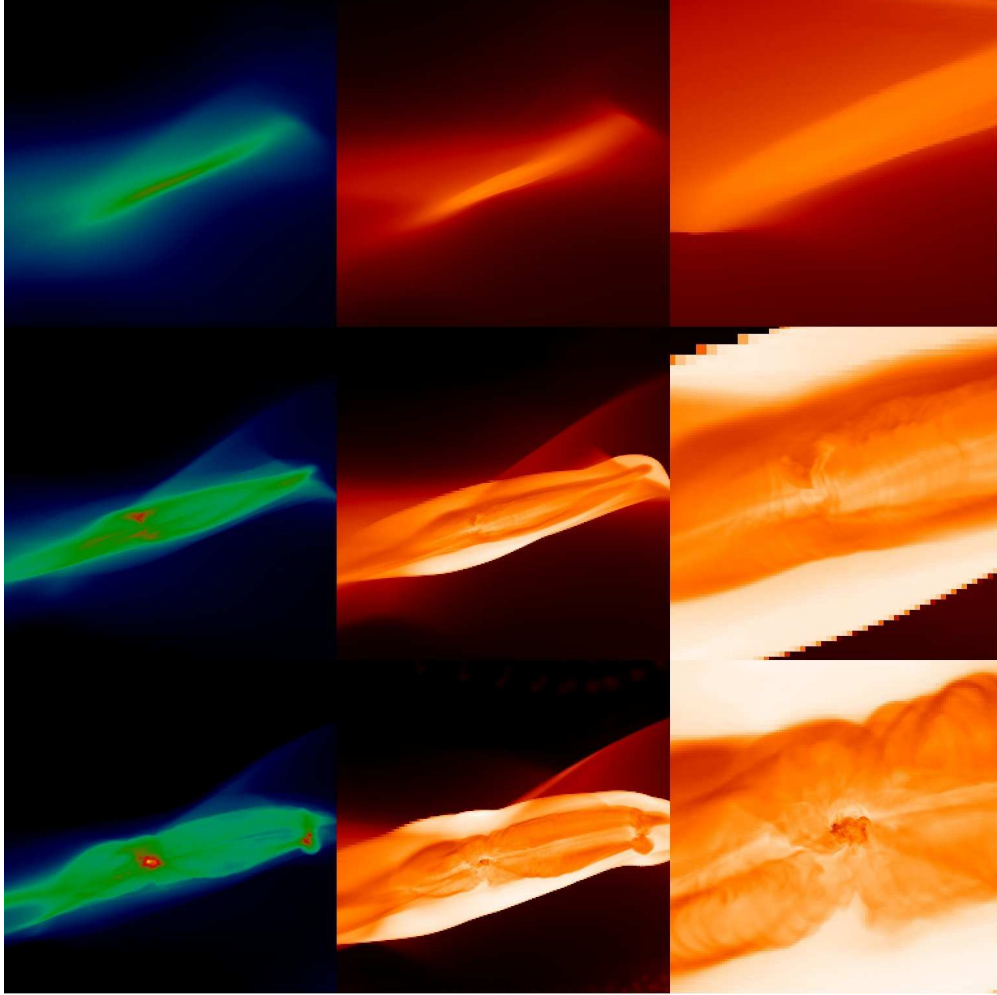


Fig. 11.— Images of baryon density and temperature as a function of redshift for the $m_{WDM} = 12.5$ keV simulation. Left column: projected baryon density. Central and right columns: projected, mass-weighted baryon temperature. Top row: quantities at $z = 15.838$. Center row: quantities at $z = 13.480$ (62.4 Myrs after top row). Bottom row: quantities at $z = 12.091$ (112.7 Myr after top row). The two left columns correspond to a proper spatial scale of $\simeq 1.5$ kpc at $z = 16$, while the right column is a zoom into the region where the Population III protostar will form, and has a proper spatial scale of $\simeq 350$ pc at $z = 16$. All projections are along the same axis of the simulation. Image colors in a given column correspond to the same baryon quantity in all panels.

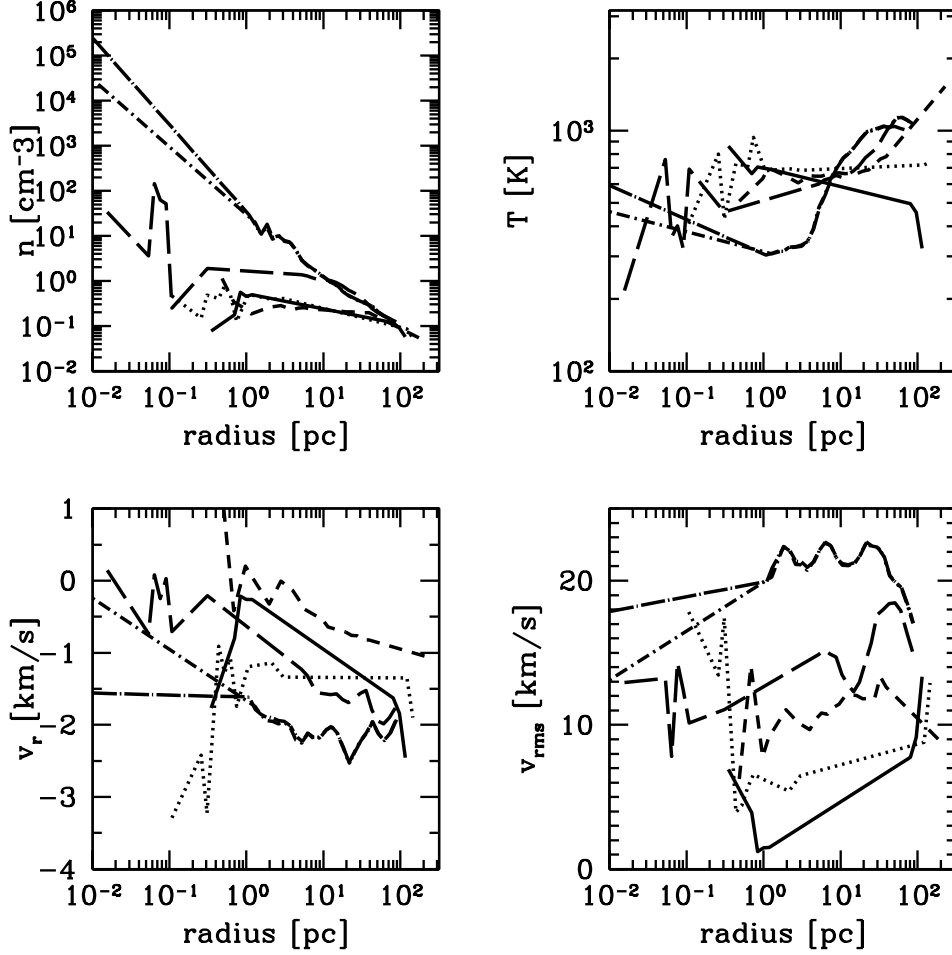


Fig. 12.— Cylindrically-averaged, mass-weighted radial profiles of baryon quantities during filament collapse in the $m_{\text{WDM}} = 12.5$ keV simulation. Top left panel: baryon number density as a function of radius. Top right panel: baryon temperature as a function of radius. Bottom left panel: baryon radial velocity as a function of radius. Bottom right panel: baryon 3D RMS velocity as a function of radius. Lines in each panel correspond to identical times. Solid line: $z = 15.838$. Dotted line: $z = 14.950$. Short-dashed line: $z = 13.48$. Long-dashed line: $z = 12.308$. Dot-short-dashed line: $z = 12.092$. Dot-long-dashed line: $z = 12.091$. At each time the center of the cylinder is the maximum point of baryon density in the collapsing halo.

can result in unphysical halos along filaments, giving the appearance of “beads on a string,” and producing an unreliable halo satellite mass function. They suggest using “glass” initial conditions (White 1996) to alleviate these problems. While we do not use a glass distribution to initialize our calculations, we are interested only in the most massive halo in the simulation, not the overall or satellite halo distributions, and this effect is unimportant for our result. Similarly, Heitmann et al. (2006) explore the evolution of the halo mass function at high redshifts, and conclude that the overall mass function is suppressed in simulations whose initial conditions are generated at too late of a redshift. They suggest that a starting simulation redshift of $z \simeq 500$ would be appropriate for the small boxes used in the calculations discussed in this paper. This is impractical for simulations containing baryonic physics, and the magnitude of error involved in simulations starting later is not quantified. Since our focus is only on the most massive halo to form in the simulation volume, the magnitude of the bias in our results by starting at $z = 100$ is unclear.

In this paper, we consider the effects of a gravitino warm dark matter power spectrum, as given by Bode et al. (2001). The other viable warm dark matter candidate, sterile neutrinos, will produce a different power spectrum at small scales for a given particle mass, which will alter our results (Abazajian 2005b). However, the two WDM candidates both have similar behavior (exponential suppression of power at small scales) so our result may have some applicability to the sterile neutrino, with some rescaling of masses. However, sterile neutrinos may have secondary effects which cloud the primary issues being examined in this work: Biermann & Kusenko (2006) suggest that decaying sterile neutrinos in the early universe may produce a relatively high level of global ionization compared to the standard case ($f_e \sim 10^{-2}$ instead of $\sim 10^{-4}$), which would serve to significantly increase molecular hydrogen production and possibly make Population III star formation more effective. A gravitino model avoids these secondary effects, and allows us to concentrate on more general issues. A further improvement upon this work would be to use power spectra for the sterile neutrino candidate, and to include their secondary effects.

There are other examples of particles that may cause suppression of small-scale power, such as superweakly interacting particles (“SuperWIMPs”) (Cembranos et al. 2005) or composite dark matter (Khlopov 2006). It is claimed that these particles may also provide solutions to the small-scale issues with structure formation. These claims are testable in cosmological simulations, and would be an obvious extension to the results presented in this paper.

Once the baryons in all of the warm dark matter simulations reach significantly high densities ($n_b \sim 10^5 \text{ cm}^{-3}$), the halo core collapses nearly identically. This is because, when the core of the halo effectively decouples from the cosmological halo (i.e. $t_{dyn}, t_s \ll t_H$, where

t_{dyn} , t_s and t_H are the dynamical and sound crossing times of the halo core and the Hubble time, respectively) the evolution of the core is driven by gas chemistry and cooling physics, which is not affected by the cosmological model. This is seen in calculations of Population III star formation in a Λ CDM universe, where a wide range of halo masses and formation times are sampled with similar results (O’Shea and Norman 2006, in preparation).

Current observations do not probe structure formation in the regime considered in this paper. The most ambitious ground- and space-based telescopes which are currently being planned or are under construction will not be able to directly observe individual Population III stars, even if they are quite massive, due to their extremely small angular size and large cosmological distance. This suggests that the most appropriate way to probe early structure formation may be by studying reionization. Future CMB experiments, such as the PLANCK mission², as well as observations of redshifted 21 cm line emission will show how and when the universe was reionized, and may give us clues as to which cosmological model is more correct (Kaplinghat et al. 2003). Reionization may be complex (e.g. Cen (2003)), and these observations may need more advanced simulations to disentangle the effects of Population III and later structures. This has been partially done numerically by Sokasian et al. (2003) and Yoshida et al. (2003b) but needs to be expanded to include a larger range of possible dark matter (e.g. linear power spectrum) models. It must be noted that all of our discussion of constraints on early universe structure formation by examining an early epoch reionization are predicated upon the assumption that this reionization was due to stars, rather than, e.g., sterile neutrino decay (Hansen & Haiman 2004).

Warm dark matter models are somewhat analogous to CDM calculations with a soft UV background, in that both cause an overall delay in collapse of the halo core and result in halos with a somewhat larger virial mass (corresponding to the later collapse time). This is due to different physical reasons, of course. One striking difference in the warm dark matter calculations is that for WDM particle masses below $\simeq 15$ keV, the suppression mass is actually at the mass of the halo in which the primordial protostar forms (at a few times $10^5 M_\odot$) so a different paradigm for structure formation occurs: the halos at this scale may form by top-down fragmentation of larger objects rather than bottom-up formation via hierarchical mergers. Remarkably, this does not appear to strongly impact the Population III initial mass function.

In principle, examination of the delay in halo collapse could allow us to suggest a new constraint on the gravitino particle mass by comparing to measurements of the reionization history of the universe. However, even the lowest gravitino mass in a simulation where the

²<http://planck.esa.int/>

halo collapsed, $M_{WDM} = 12.5$ keV, is still consistent with the WMAP Year 3 polarization measurement. Given the small box size and the problems inherent in extrapolating the reionization history of the universe from a single object, this should not be taken as any sort of useful limit. In order to provide a more plausible limit to the gravitino particle mass, simulations of much larger cosmological volumes must be run and the inferred reionization histories compared to future CMB and 21 cm observations.

5. Summary of results

In this paper we have performed a series of simulations of structure formation in the early universe in an attempt to provide more stringent constraints on a possible warm dark matter particle mass and to examine how the suppression of small-scale power affects the formation of protostellar cores. We use an identical cosmological realization, but apply smoothing to the initial conditions according to the WDM transfer function given by Bode et al. (2001), for a range of warm dark matter particle masses which have not yet been observationally ruled out. Our principal conclusions are as follows:

1. We find that, for a wide range of warm dark matter particle masses, the main effect of the smoothing of small-scale power is to delay the collapse of high-density gas at the center of the most massive halo in the simulation and, as a result, an increase in the virial mass of this halo at the onset of baryon collapse. Both of these effects become more pronounced as the warm dark matter particle mass becomes smaller.

2. A cosmology using a warm dark matter particle mass of $\simeq 40$ keV is effectively indistinguishable from the cold dark matter case, making this a reasonable upper limit of gravitino masses that have any significant effect on large scale structure (though providing no useful particle physics constraints on the mass of such a particle).

3. There is remarkably little scatter in the final properties of the primordial protostellar core which forms at the center of the halo, possibly due to the overall low rate of halo mergers which is a result of the warm dark matter power spectrum.

4. The detailed evolution of the collapsing halo core in two representative warm dark matter cosmologies is described. At relatively low densities ($n_b \lesssim 10^5 \text{ cm}^{-3}$) the evolution of the two calculations is similar, but the calculation with a lower particle mass takes a much longer amount of time to reach the runaway collapse phase. Once the gas in the center of the halo reaches higher densities ($n_b \gtrsim 10^5 \text{ cm}^{-3}$), the overall evolution is essentially identical in the two calculations, implying that the mass of the warm dark matter particle should not affect the Population III initial mass function, assuming that the particle mass is small

enough to allow prototypical Population III halos to still form.

BWO would like to thank Kevork Abazajian, Tom Abel, Greg Bryan, Salman Habib, Katrin Heitmann, and Matthew Turk for useful discussions. We would like to thank an anonymous referee who made several suggestions which have improved the quality of this manuscript. This work was supported in part by NASA grant NAG5-12140 and NSF grant AST-0307690. BWO has been funded in part under the auspices of the U.S. Dept. of Energy, and supported by its contract W-7405-ENG-36 to Los Alamos National Laboratory. The simulations were performed at SDSC and NCSA with computing time provided by NRAC allocation MCA98N020.

REFERENCES

- Abazajian, K. 2005a, PRD, submitted; astro-ph/0512631
- . 2005b, PRD, submitted; astro-ph/0511630
- Abazajian, K., Fuller, G. M., & Tucker, W. H. 2001, *ApJ*, 562, 593
- Abel, T., Anninos, P., Zhang, Y., & Norman, M. L. 1997, *New Astronomy*, 2, 181
- Abel, T., Bryan, G. L., & Norman, M. L. 2002, *Science*, 295, 93
- Anninos, P., Zhang, Y., Abel, T., & Norman, M. L. 1997, *New Astronomy*, 2, 209
- Bahcall, N. A., Ostriker, J. P., Perlmutter, S., & Steinhardt, P. J. 1999, *Science*, 284, 1481
- Bardeen, J. M., Bond, J. R., Kaiser, N., & Szalay, A. S. 1986, *ApJ*, 304, 15
- Barkana, R., Haiman, Z., & Ostriker, J. P. 2001, *ApJ*, 558, 482
- Barkana, R. & Loeb, A. 2004, *ApJ*, 609, 474
- Berger, M. J. & Colella, P. 1989, *J. Comp. Phys.*, 82, 64
- Biermann, P. & Kusenko, A. 2006, astro-ph/0601004
- Bode, P., Ostriker, J. P., & Turok, N. 2001, *ApJ*, 556, 93
- Bromm, V., Coppi, P. S., & Larson, R. B. 2002, *ApJ*, 564, 23

- Bryan, G. & Norman, M. 1997a, 12th Kingston Meeting on Theoretical Astrophysics, proceedings of meeting held in Halifax; Nova Scotia; Canada October 17-19; 1996 (ASP Conference Series # 123), ed. D. Clarke. & M. Fall
- . 1997b, Workshop on Structured Adaptive Mesh Refinement Grid Methods, ed. N. Chrochoides (IMA Volumes in Mathematics No. 117)
- Bryan, G. L., Norman, M. L., Stone, J. M., Cen, R., & Ostriker, J. P. 1995, *Comp. Phys. Comm*, 89, 149
- Cembranos, J. A., Feng, J. L., Rajaraman, A., & Takayama, F. 2005, *Physical Review Letters*, 95, 181301
- Cen, R. 2003, *ApJ*, 591, 12
- Chiba, M. 2002, *ApJ*, 565, 17
- Colombi, S., Dodelson, S., & Widrow, L. M. 1996, *ApJ*, 458, 1
- Dalal, N. & Kochanek, C. S. 2002, *ApJ*, 572, 25
- Dalcanton, J. J. & Hogan, C. J. 2001, *ApJ*, 561, 35
- Efstathiou, G., Davis, M., White, S. D. M., & Frenk, C. S. 1985, *ApJS*, 57, 241
- Eisenstein, D. J. & Hu, W. 1999, *ApJ*, 511, 5
- Eisenstein, D. J. & Hut, P. 1998, *ApJ*, 498, 137
- Ghigna, S., Moore, B., Governato, F., Lake, G., Quinn, T., & Stadel, J. 2000, *ApJ*, 544, 616
- Götz, M. & Sommer-Larsen, J. 2003, *Ap&SS*, 284, 341
- Governato, F., Mayer, L., Wadsley, J., Gardner, J. P., Willman, B., Hayashi, E., Quinn, T., Stadel, J., et al. 2004, *ApJ*, 607, 688
- Hansen, S. H. & Haiman, Z. 2004, *ApJ*, 600, 26
- Heitmann, K., Lukic, Z., Habib, S., & Ricker, P. M. 2006, *ArXiv Astrophysics e-prints*
- Hockney, R. W. & Eastwood, J. W. 1988, *Computer Simulation Using Particles* (Institute of Physics Publishing)
- Kaplinghat, M., Chu, M., Haiman, Z., Holder, G. P., Knox, L., & Skordis, C. 2003, *ApJ*, 583, 24

- Khlopov, M. Y. 2006, *Pisma Zh.Eksp.Teor.Fiz.*, 83, 3
- Klypin, A., Kravtsov, A. V., Valenzuela, O., & Prada, F. 1999, *ApJ*, 522, 82
- Knebe, A., Devriendt, J. E. G., Gibson, B. K., & Silk, J. 2003, *MNRAS*, 345, 1285
- Kogut, A., Spergel, D. N., Barnes, C., Bennett, C. L., Halpern, M., Hinshaw, G., Jarosik, N., Limon, M., et al. 2003, *ApJS*, 148, 161
- Kormendy, J. & Fisher, D. B. 2005, in *Revista Mexicana de Astronomia y Astrofisica Conference Series*, 101–108
- Kravtsov, A. V., Gnedin, O. Y., & Klypin, A. A. 2004, *ApJ*, 609, 482
- Machacek, M. E., Bryan, G. L., & Abel, T. 2001, *ApJ*, 548, 509
- Metcalfe, N., Shanks, T., Campos, A., McCracken, H. J., & Fong, R. 2001, *MNRAS*, 323, 795
- Minchin, R., Davies, J., Disney, M., Boyce, P., Garcia, D., Jordan, C., Kilborn, V., Lang, R., et al. 2005, *ApJ*, 622, L21
- Moore, B., Ghigna, S., Governato, F., Lake, G., Quinn, T., Stadel, J., & Tozzi, P. 1999a, *ApJ*, 524, L19
- Moore, B., Quinn, T., Governato, F., Stadel, J., & Lake, G. 1999b, *MNRAS*, 310, 1147
- Narayanan, V. K., Spergel, D. N., Davé, R., & Ma, C.-P. 2000, *ApJ*, 543, L103
- Navarro, J. F., Frenk, C. S., & White, S. D. M. 1997, *ApJ*, 490, 493
- Navarro, J. F., Hayashi, E., Power, C., Jenkins, A. R., Frenk, C. S., White, S. D. M., Springel, V., Stadel, J., et al. 2004, *MNRAS*, 349, 1039
- Norman, M. & Bryan, G. 1999, *Numerical Astrophysics : Proceedings of the International Conference on Numerical Astrophysics 1998 (NAP98)*, held at the National Olympic Memorial Youth Center, Tokyo, Japan, March 10-13, 1998., ed. K. T. S. M. Miyama & T. Hanawa (Kluwer Academic)
- Omukai, K. & Palla, F. 2003, *ApJ*, 589, 677
- O’Shea, B., Bryan, G., Bordner, J., Norman, M., Abel, T., & Harkness, R. and Kritsuk, A. 2004, *Adaptive Mesh Refinement - Theory and Applications*, ed. T. Plewa, T. Linde, & G. Weirs (Springer-Verlag)

- O’Shea, B. W., Nagamine, K., Springel, V., Hernquist, L., & Norman, M. L. 2005, *ApJS*, 160, 1
- Page, L., Hinshaw, G., Komatsu, E., Nolta, M. R., Spergel, D. N., Bennett, C. L., Barnes, C., Bean, R., et al. 2006, *ArXiv Astrophysics e-prints*
- Peebles, P. J. E. 1968, *ApJ*, 153, 1
- . 2001, *ApJ*, 557, 495
- Percival, W. J., Baugh, C. M., Bland-Hawthorn, J., Bridges, T., Cannon, R., Cole, S., Colless, M., Collins, C., et al. 2001, *MNRAS*, 327, 1297
- Ripamonti, E. & Abel, T. 2004, *MNRAS*, 348, 1019
- Schaerer, D. 2002, *A&A*, 382, 28
- Sokasian, A., Abel, T., Hernquist, L., & Springel, V. 2003, *MNRAS*, 344, 607
- Somerville, R. S., Bullock, J. S., & Livio, M. 2003, *ApJ*, 593, 616
- Sommer-Larsen, J. & Dolgov, A. 2001, *ApJ*, 551, 608
- Stone, J. M. & Norman, M. L. 1992a, *ApJS*, 80, 753
- . 1992b, *ApJS*, 80, 791
- Swaters, R. A., Madore, B. F., & Trewhella, M. 2000, *ApJ*, 531, L107
- Tegmark, M., Blanton, M. R., Strauss, M. A., Hoyle, F., Schlegel, D., Scoccimarro, R., Vogeley, M. S., Weinberg, D. H., et al. 2004, *ApJ*, 606, 702
- Tegmark, M., Silk, J., Rees, M. J., Blanchard, A., Abel, T., & Palla, F. 1997, *ApJ*, 474, 1
- Truelove, J. K., Klein, R. I., McKee, C. F., Holliman, J. H., Howell, L. H., & Greenough, J. A. 1997, *ApJ*, 489, L179+
- van den Bosch, F. C., Robertson, B. E., Dalcanton, J. J., & de Blok, W. J. G. 2000, *AJ*, 119, 1579
- Viel, M., Lesgourgues, J., Haehnelt, M. G., Matarrese, S., & Riotto, A. 2005, *Phys. Rev. D*, 71, 063534
- White, S. D. M. 1996, in *Cosmology and Large Scale Structure*, 349–+

- Willman, B., Governato, F., Dalcanton, J. J., Reed, D., & Quinn, T. 2004, MNRAS, 353, 639
- Woodward, P. R. & Colella, P. 1984, J. Comp. Phys., 54, 174
- Yoshida, N., Abel, T., Hernquist, L., & Sugiyama, N. 2003a, ApJ, 592, 645
- Yoshida, N., Sokasian, A., Hernquist, L., & Springel, V. 2003b, ApJ, 591, L1